

Tilt and strain change during the explosion at Minami-dake, Sakurajima, on November 13, 2017

Kohei Hotta (✉ hotta@sus.u-toyama.ac.jp)

Faculty of Sustainable Design, University of Toyama <https://orcid.org/0000-0001-8968-0038>

Masato Iguchi

Disaster Prevention Research Institute, Kyoto University

Full paper

Keywords: Sakurajima volcano, Spherical source, Dike, Tilt, Strain

Posted Date: January 26th, 2021

DOI: <https://doi.org/10.21203/rs.3.rs-108518/v2>

License:   This work is licensed under a Creative Commons Attribution 4.0 International License.

[Read Full License](#)

Version of Record: A version of this preprint was published on March 16th, 2021. See the published version at <https://doi.org/10.1186/s40623-021-01392-6>.

1 **Title page:**

2

3 **Title: Tilt and strain change during the explosion at Minami-dake, Sakurajima, on**

4 **November 13, 2017**

5 Author #1: Kohei Hotta, Faculty of Sustainable Design, University of Toyama, Toyama

6 930-8555, Japan, hotta@sus.u-toyama.ac.jp

7 Author #2: Masato Iguchi, Masato Iguchi, Sakurajima Volcano Research Center, Disaster

8 Prevention Research Institute, Kyoto University, Kagoshima 891-1419, Japan,

9 iguchi.masato.8m@kyoto-u.ac.jp

10

11 Corresponding author: Kohei Hotta, hotta@sus.u-toyama.ac.jp

12

13 **Abstract**

14 We herein propose an alternative model for deformation caused by an eruption at
15 Sakurajima, which have been previously interpreted as being due to a Mogi-type spherical
16 point source beneath Minami-dake. On November 13, 2017, a large explosion with a
17 plume height of 4,200 m occurred at Minami-dake. During the three minutes following
18 the onset of the explosion (November 13, 2017, 22:07–22:10 (Japan standard time
19 (UTC+9); the same hereinafter), phase 1, a large strain change was detected at the
20 Arimura observation tunnel (AVOT) located approximately 2.1 km southeast from the
21 Minami-dake crater. After the peak of the explosion (November 13, 2017, 22:10–24:00),
22 phase 2, a large deflation was detected at every monitoring station due to the continuous
23 Strombolian eruption. Subsidence toward Minami-dake was detected at five out of six
24 stations whereas subsidence toward the north of Sakurajima was detected at the newly
25 installed Komen observation tunnel (KMT), located approximately 4.0 km northeast from
26 the Minami-dake crater. The large strain change at AVOT as well as small tilt changes of
27 all stations and small strain changes at HVOT and KMT during phase 1 can be explained
28 by a very shallow deflation source beneath Minami-dake at 0.1 km below sea level (bsl).
29 For phase 2, a deeper deflation source beneath Minami-dake at a depth of 3.3 km bsl was
30 found in addition to the shallow source beneath Minami-dake which turned inflation after
31 the deflation obtained during phase 1. However, this model cannot explain the tilt change
32 of KMT. Adding a spherical deflation source beneath Kita-dake at a depth of 3.2 km bsl
33 can explain the tilt and strain change at KMT and the other stations. The Kita-dake source
34 was also found in a previous study of long-term ground deformation. Not only the deeper
35 Minami-dake source M_D but also the Kita-dake source deflated due to the Minami-dake
36 explosion.

37

38 **Keywords**

39 Sakurajima volcano, Spherical source, Dike, Tilt, Strain

40

41 **1. Introduction**

42 The tilt and strain changes accompanying vulcanian eruptions of Sakurajima have
43 been interpreted as being due to the deflation of a Mogi-type source (Mogi, 1958) beneath
44 Minami-dake, because downward tilts associated with eruptions are oriented towards
45 Minami-dake in the underground tunnels Harutayama (2.7 km northwest of the Minami-
46 dake crater) and Arimura (2.1 km south-southeast of the crater) (Fig. 1). As for eruptions
47 at Minami-dake started in 1955, a deflation source was found beneath Minami-dake at a
48 depth of 2–4 km below sea level (bsl), with a deflation volume of 10^3 – 10^5 m³. This source
49 was also found during an episode of frequent vulcanian eruptions at Minami-dake that
50 peaked from 1974 to 1992 by precise leveling surveys (Eto, 1989). A shallower deflation
51 source was also found at the onset of the eruption (e.g., Ishihara, 1990; Iguchi et al., 2013).
52 As for eruptions at Showa crater started in 2006, only a shallower deflation source was
53 found beneath Minami-dake at a depth of 0–1.5 km bsl, with a deflation volume of 10^2 –
54 10^4 m³, one-order smaller than that of Minami-dake eruptions. (Iguchi et al., 2013).
55 During an episode of eruptions at Showa crater, a different source was found beneath
56 Kita-dake at a depth of 3.3 km bsl by continuous GPS observation data. This source was
57 considered to be repeating inflation and deflation with a period of several years (Hotta et
58 al., 2016a). In August 2016, additional tilt and strain observations were undertaken at a
59 new observation tunnel at Komen, 4.0 km northeast of Minami-dake, and changes were
60 detected, associated with a large explosion with a plume height of 4,200 m at Minami-

61 dake on November 13, 2017. More than one year had passed since installation of
62 tiltmeters and strainmeters in Komen observation tunnel when the eruption occurred.
63 Ground inflation started at 8:00 (Japan standard time (UTC+9); the same hereinafter) on
64 November 7, 2017, which became a gradual deflation on November 11, 2017. When an
65 explosion occurred at 22:07 of November 13, 2017, the gradual deflation became rapid
66 and continued for two hours. The total duration of tilt/strain change of nearly a week is
67 longer than the typical eruptions at Minami-dake in 1980s of at most seven hours (Ishihara,
68 1990). The downward tilt direction at the Komen tunnel deviated by 90° clockwise from
69 the direction of the Minami-dake crater, in a different manner than at the Arimura and
70 Harutayama tunnels, which showed a downward tilt in the direction of the crater. This tilt
71 direction is substantially different from the deformation expected from the inflation of the
72 Mogi-type spherical point source beneath Minami-dake found in previous studies, and
73 thus the deformation at the Komen tunnel is affected by a different source.

74 In the present study, we propose a composite source model for tilt and strain changes
75 at ground deformation stations, taking into account the tilt change at the Komen tunnel.
76 We then discuss the magma plumbing system of Sakurajima for a large-scale vulcanian
77 eruption.

78

79 **2. Observations and data**

80 At Sakurajima, tilt and strain observations have been performed by the Sakurajima
81 Volcano Research Center (SVRC) of Kyoto University; the Osumi Office of River and
82 National Development Bureau, Ministry of Land, Infrastructure, Transport and Tourism
83 of Japan (MLIT); and the Japan Meteorological Agency (JMA). The tilt and strain stations
84 for the present study are distributed as shown in Fig. 1. We used data obtained by water-

85 tube tiltmeters and linear strainmeters at the Arimura, Harutayama and Komen
86 underground tunnels (AVOT, HVOT and KMT, respectively) and borehole tiltmeters at
87 Yokoyama, Amida-gawa and Komen (JMA-A, JMA-F and KOM, respectively). The
88 tiltmeters and strainmeters at AVOT, HVOT, KMT and KOM were installed in directions
89 radial and tangential to Minami-dake and the tiltmeters at JMA-A and F were in the north-
90 south and east-west directions. The sensitivities were 0.056 V/ μ rad for the water-tube
91 tiltmeters and 0.056 V/ μ strain for the linear strainmeters. The sensitivity of the borehole
92 tiltmeters was 0.02 V/ μ rad. The analog-to-digital resolution was 24 bits and the resolution
93 of tilt and strain was 10^{-6} nrad.

94 The tilt and strain changes at AVOT, HVOT and KMT during the period of November
95 5–14, 2017, are shown in Fig. 2. Upward tilts in the direction of Minami-dake and
96 extension strains started to appear at about 6:00 of November 7 at AVOT and HVOT,
97 whereas a tangential tilt was dominant at KMT. The tilts turned to gradual downward tilts
98 on November 11, 2017. Then, the downward tilt suddenly became rapid at the onset of
99 the explosion on November 13. A deflation tilt change of 283 nrad occurred over two
100 hours at HVOT, which is larger than the tilt changes associated with explosions at
101 Minami-dake crater in the previous reports (Ishihara, 1990; Tateo and Iguchi, 2009).

102 The tilt and strain changes associated with the explosion are magnified in Fig.3. In
103 phase 1 (three minutes from the onset of the explosion at 22:07), rapid extensions were
104 detected in the radial strains as strain steps. The step at AVOT, the nearest station to the
105 Minami-dake crater, is the largest at 120 nstrain, and the steps are smaller at the farther
106 tunnels HVOT and KMT. In phase 2 (22:10–24:00), a large deflation with a contraction
107 strain and downward tilts oriented towards the Minami-dake crater are observed, except
108 at KMT. The downward tilt vectors are shown in Fig. 4(a). The vector at KMT is oriented

109 toward the north flank of Sakurajima.

110

111 **3. Analysis**

112 **3.1. Deformation source model**

113 We applied a finite spherical source (McTigue, 1987), a dislocation source (Okada,
114 1992) and a combination of these in a half-infinite homogenous elastic solid. We assumed
115 a Poisson's coefficient of $\nu = 0.25$. Battaglia et al. (2013) obtained the volume change
116 of a spherical source ΔV by an internal pressure change of ΔP , for a modulus of rigidity
117 μ and depth and radius of the source d and a , respectively, to be

$$118 \quad \Delta V = \pi a^3 \frac{\Delta P}{\mu} \left[1 + \left(\frac{a}{d} \right)^4 \right]. \quad (1)$$

119 From equation (1), $\Delta P/\mu$ in the equations of deformation by McTigue (1987) can be
120 obtained using ΔV . Topographical effects was corrected by adding the elevation of the
121 station to the source depth (Williams and Wadge, 1998).

122 To expand the original elastic source models described above to a multiple-source
123 model, we assumed that the sources do not interact with each other and that the calculated
124 tilt and strain are linear sums of the tilt and strains caused by the sources (Hotta et al.,
125 2016a).

126

127 **3.2. Residual evaluation**

128 We searched for the optimal parameters for each source (Table 1) using a grid search
129 method. For models with more than seven parameters, composite model of a tensile fault
130 and dual spherical source, we used a genetic algorithm (e.g., Tiampo et al., 2000) instead
131 of a grid search method. In this case, we set the number of individuals to be 50; the
132 probabilities of crossovers, jump mutations and creep mutation to be 70, 2 and 18%,

133 respectively; and the number of iterations for the genetic algorithm to be 200,000. Here,
 134 individuals have model parameter information as binary code; crossover is a random
 135 exchange of part of a binary code among an arbitrary pair of individuals; jump mutation
 136 is a random change in a bit in the binary code of an individual; and creep mutation is a
 137 ± 1 step change in model parameter information in an individual. To avoid a local
 138 minimum, we executed the iteration process several times (Hotta et al., 2016a; 2016b).
 139 To minimize the difference between the observed and theoretical values, we used the
 140 weighted residual sum of square (WRSS):

$$141 \quad \text{WRSS} = \Delta^2 + E^2, \quad (2)$$

142 where Δ^2 and E^2 are weighted residual sums of square of tilt and strain, respectively:

$$143 \quad \Delta^2 = \sum_{1 \leq i \leq 6} \left[\left(\frac{\delta R_{obs}^i - \delta R_{cal}^i}{\sigma \delta R^i} \right)^2 + \left(\frac{\delta T_{obs}^i - \delta T_{cal}^i}{\sigma \delta T^i} \right)^2 \right], \quad (3)$$

$$144 \quad E^2 = \sum_{1 \leq j \leq 3} \left[\left(\frac{\varepsilon R_{obs}^j - \varepsilon R_{cal}^j}{\sigma \varepsilon R^j} \right)^2 + \left(\frac{\varepsilon T_{obs}^j - \varepsilon T_{cal}^j}{\sigma \varepsilon T^j} \right)^2 + \left(\frac{\varepsilon O_{obs}^j - \varepsilon O_{cal}^j}{\sigma \varepsilon O^j} \right)^2 \right], \quad (4)$$

145 and where the subscripts *obs* and *cal* indicate observed and calculated values; δR^i
 146 and δT^i indicate the radial and tangential tilt change at the *i*-th tilt station, respectively;
 147 εR^j , εT^j and εO^j indicate the radial, tangential and oblique strain changes at the *j*-th
 148 observation tunnel, respectively; and σ indicates the observation error. The search
 149 spaces and step sizes for the parameter estimates are given in Table 1.

150

151 **4. Results**

152 **4.1. Phase 1**

153 A single spherical source model was determined for phase 1. Through the grid search
 154 method, we obtained a very shallow deflation source beneath Minami-dake (source Ms)
 155 at 0.1 km bsl (Fig. 4(a), Table 1). Its radius was the minimum value of the search range,

156 0.1 km. The large strain change detected at AVOT, small tilt change including AVOT and
157 strain change at the other stations can be explained by this source (Fig. 4(a) and (b)).

158

159 **4.2. Phase 2**

160 **4.2.1. Deformation sources beneath Minami-dake**

161 During phase 2, subsidence in a direction toward Minami-dake was detected except
162 at the KMT observation tunnel where a subsidence in the direction toward the north flank
163 was detected. Excluding the data of KMT, we applied dual spherical sources: a shallow
164 source (source M_S) fixed at the location obtained for phase 1 and a deep source, M_D . M_D
165 is a deeper (3.3 km bsl beneath Minami-dake) deflation source, whereas M_S causes
166 inflation as shown in Fig. 5(a) and Table 1. We note, however, that these sources beneath
167 Minami-dake cannot explain the oblique strain change at HVOT. These sources also
168 cannot explain the tilt and strain changes at the KMT observation tunnel, where
169 subsidence toward the north area of Sakurajima was detected (Fig. 5).

170

171 **4.2.2. Improvement by the addition of sources for KMT data**

172 Despite the shallow and deep Minami-dake sources can explain most tilt/strain data, there
173 are still misfits in the oblique strain change at HVOT and tilt/strain data at KMT. In the
174 period of 2011–2012, there was a source identified beneath Kita-dake (Hotta et al., 2016a),
175 as mentioned in introduction, and this source might have re-activated during the explosion
176 of Minami-dake. Thus, we added a third source and test whether it is a spherical or
177 dike/sill-like.

178 **4.2.2.1. Triple spherical source model**

179 Hotta et al (2016a) found a Mogi-type deformation source beneath Kita-dake in

180 addition to that beneath Minami-dake for the long-term deformation event of October
181 2011–March 2012. We applied a triple spherical deformation source model adding a non-
182 fixed spherical source to M_S and M_D , fixed at the locations obtained above. The new
183 source is a deflation source beneath the northeast flank of Kita-dake where an inflation
184 source was found by Hotta et al. (2016a) during the long-term deformation period from
185 October 2011 to March 2012 (Fig. 6(a); Table 1). The fit of the calculation to the observed
186 oblique strain change at HVOT and tilt and strain changes at KMT are improved by this
187 addition (Fig. 6), and WRSS value reduced from 55,494 to 13,408.

188

189 **4.2.2.2. Composite model of a tensile fault and dual spherical source**

190 Hotta et al. (2016b) applied a tensile fault model to the deformation of Sakurajima.
191 Here, we add a tensile fault to M_S and M_D . In addition to the inflation of M_S and deflation
192 of M_D , a sill with a length and width of 4.7 and 0.4 km, respectively, and striking in the
193 north-south direction is located beneath the Aira caldera where submarine eruptions
194 occurred around this area during the An'ei eruption in 1779 at a depth of 0.7 km bsl (Fig.
195 7(a), Table 1). The fit of the calculation to the observed oblique strain change at HVOT
196 and tilt and strain changes at KMT are improved by this addition (Fig. 7), and WRSS
197 value reduced from 55,494 to 9,140.0.

198

199 **5. Discussion** **5.1. Selection of the optimal model for phase 2**

200 To select an optimum model, for each model we evaluated the correction of Akaike's
201 Information Criterion (c-AIC) values (Sugiura, 1978), which is a finite correction of
202 Akaike's Information Criterion (AIC; Akaike, 1973). The WRSS values of the three
203 spherical sources and the dual spherical sources with tensile fault models are 13,408 and

204 9,140.0, respectively, and the number of free parameters is seven and ten, respectively.
205 These yield c-AIC values of 222.19 and 233.53, respectively. Although the residual is
206 larger than the dual spherical sources with a tensile fault model, the three spherical
207 sources model is better, based on the obtained c-AIC values. In another respect, volume
208 increase of obtained tensile fault is nearly 10^7 m³/(1.83 hours), which is too large from
209 the point of view of the typical magma intrusion rate of Sakurajima, 10^7 m³/year (Ishihara,
210 1981). Therefore, we concluded that the three spherical sources model is the optimal
211 model for phase 2.

212 As for a finite spherical source model, Pascal et al. (2014) noted that the effect of
213 interaction between sources is negligible when sources are separated by four or more radii.
214 The distance between sources M_S and M_D is 3.6 km, that between M_D and K is 4.8 km,
215 and that between K and M_S is 5.7 km. Meanwhile, radii of M_S, M_D and K are 0.1 km, 0.5
216 km and 0.1 km, respectively. From these distances and radii, these three spherical sources
217 separate enough to ignore the effect of interaction between them.

218

219 **5.2. Interpretations of the sources**

220 During the three minutes from the onset of the explosion at 22:07, phase 1, a very
221 shallow deflation source was obtained beneath Minami-dake, similar to previous
222 eruptions at the Minami-dake (Ishihara, 1990) and Showa craters (Iguchi et al., 2013).
223 This means that the deflation starts from a shallow part of the magma plumbing system
224 of Sakurajima. This shallow source might represent uppermost part of magma conduit
225 from deeper Minami-dake source to summit crater which have been interpreted as high-
226 pressure gas chamber (e.g., Iguchi, 1994). After the peak of the vulcanian eruption, phase
227 2, the deeper source beneath Minami-dake deflated while the shallower source inflated.

228 The deep deflation source beneath Minami-dake had been identified based on tilt and
229 strain changes during previous eruptions at the Minami-dake and Showa craters. The
230 obtained depth of 3.3 km bsl was comparable with previous studies (2–4 km), and
231 horizontal location of the source was similar to the fixed location of previous studies,
232 beneath Minami-dake (e.g., Ishihara, 1990; Iguchi et al., 2013). In addition to the deeper
233 source, inflation of the shallower source was detected. The shallow inflation source
234 beneath Minami-dake found in the present study was not found in the previous studies.
235 During the Minami-dake eruption including this event, the shallower source is considered
236 to deflate for the first phase of each eruption. In this event, the shallower source inflated
237 after the peak of the explosion probably because the amount of accumulation of magma
238 from the deeper source exceeds that of the emission from the Minami-dake crater due to
239 continuous Strombolian eruptions (Fig. 8). In addition to the two Minami-dake sources,
240 we found a deflating spherical source at a depth of 3.2 km bsl at the northeastern flank of
241 Kita-dake. The Kita-dake source might correspond to the source K found beneath Kita-
242 dake at a depth of 3.3 km bsl from a combination analysis of GPS, tilt and strain data
243 during the period from October 2011 to March 2012 (Hotta et al., 2016a). The Kita-dake
244 source was also found based on vertical displacement during the period from November
245 2008 to November 2009, obtained from a precise leveling survey (Yamamoto et al., 2013).
246 Not only the deeper Minami-dake source M_D but also the Kita-dake source deflated due
247 to the Minami-dake explosion (Fig. 8) The total deflation volume of sources M_D and K
248 was $88,900 \text{ m}^3$, which is comparable with the previous Minami-dake eruptions of 10^3 –
249 10^5 m^3 (Ishihara, 1990).

250 A clear reflector at a depth of 5.8 km bsl beneath Kita-dake, identified as an
251 overcritical PP reflection, was found by seismic experiments during the period from

252 December 2009 to December 2014. The reflection became clear in December 2014, and
253 the reflector was interpreted as a sill (Tsutsui et al., 2016). The source K obtained in the
254 present study is shallower than the reflector, but the horizontal location is similar. The
255 99% confidence interval of the depth of source K is 2.6–5.8 km bsl, as shown in Table 1,
256 and the depths of source K and the reflector may overlap considering the uncertainty in
257 the depth of the reflector of ± 90 m (Tsutsui, personal communication on December 17,
258 2020). If source K and the reflector are the same, the difference in the optimal depth may
259 be due to the source shape, such as a penny shaped source (Fialco et al., 2001). This
260 should be considered in future studies.

261

262 **5.3. Affection of topography and heterology**

263 There are a lot of limitations such as topography and heterogeneity in an elastic model
264 we used in the present study (e.g., Del Negro et al., 2009; Gottsmann and Odbert, 2014;
265 Hickey et al., 2016). Although realistic modeling using finite element method (FEM) is
266 time consuming, we at least tried to check affection of volume change for phase 2. We
267 applied an FEM using the software Flex PDE Professional version 6.50 provided by PDE
268 Solutions Inc. We set an FEM domain size of $100 \times 100 \times 50$ km³ (130.13325–
269 131.18675°E, 31.12906–32.03094°N, 0–50 km bsl). We set top of the domain as a free
270 surface, and sides and bottom of the domain as fixed boundaries. Topography was
271 introduced in the area within Sakurajima using digital elevation model (DEM) data with
272 100 m resolution, and elevation of the outside area was assumed to be sea level.
273 Heterogeneity of P-wave velocity was introduced referring to Miyamachi et al. (2013) as
274 1, 2.5, 3.6, 4.8 and 6 km/s for the depth range of 0–0.2, 0.2–1, 1–2, 2–3 and 3– km from
275 the surface, respectively. Assuming a Poisson's ratio as 0.25 and V_p/V_s velocity ratio as

276 1.73, modulus of rigidity μ can be written using the density of ground ρ as

$$277 \quad \mu = \frac{\rho V_p^2}{3}. \quad (5)$$

278 Currenti et al. (2007) found the following empirical formula between the density of
279 ground and P-wave velocity:

$$280 \quad \rho = 1.2861 + 0.5498V_p - 0.0930V_p^2 + 0.007V_p^3. \quad (6)$$

281 From eqs. (5) and (6), modulus of rigidity of the P-wave velocity structure can be
282 calculated as 1.02, 3.99, 6.84, 10.5 and 15.1 GPa for the depth range of 0–0.2, 0.2–1, 1–
283 2, 2–3 and 3– km from the surface, respectively. Using the FEM domain described above,
284 we first calculated tilt and strain change due to pressure change of +1 MPa inside each
285 source of M_s , M_D and K , fixing horizontal location, depth and radius obtained using an
286 elastic model. We then searched the optimal internal pressure change by grid search
287 method based on the fact that tilt/strain changes are proportionate to internal pressure
288 change in FEM calculation. The search range and step were set to be –100–+100 MPa
289 and 0.01 MPa, respectively. The optimal internal pressure changes of sources M_s , M_D and
290 K was +0.71 MPa, –1.41 MPa and –82.98 MPa, respectively. These yield volume changes
291 of +450 m³, –36,200 m³ and –16,700 m³, respectively. The yielded WRSS value of 15,997
292 was slightly larger than that of elastic model, but data can be well explained (Fig. 9). All
293 of the yielded volume change amounts were smaller compared to these obtained using
294 elastic model, especially the shallowest source M_s which was out of the estimated 99%
295 confidence interval of elastic model, 600–5,000 m³. This means modeling by an elastic
296 model leads overestimate of volume change, particularly for the shallow source. The
297 overestimate of volume change could be also caused by compression of magma (Rivalta
298 and Segall, 2008).

299 This time, we checked only for volume change. We need to check for location, depth

300 and radius of the source as well in the future study.

301

302 **6. Conclusions**

303

304 We modeled tilt and strain change during the eruption at Minami-dake on November
305 13, 2017 by an elastic model. During the three minutes from the onset of the explosion at
306 22:07, a shallow source beneath Minami-dake was deflated, which was interpreted as
307 uppermost part of magma conduit from deeper Minami-dake source to summit crater.
308 After the peak of the vulcanian eruption, the deeper source beneath Minami-dake deflated
309 while the shallower source inflated. The deep deflation source beneath Minami-dake had
310 been identified based on tilt and strain changes during previous eruptions at the Minami-
311 dake and Showa craters. Inflation of the shallower source may be caused because the
312 amount of accumulation of magma from the deeper source exceeds that of the emission
313 from the Minami-dake crater due to continuous Strombolian eruptions. In addition, a
314 deflating spherical source beneath Kita-dake was also found, which was identified during
315 the long-term deformation event in 2011–2012. We found that the Kita-dake source,
316 which was considered to be repeating inflation and deflation with a period of several years,
317 may also cause deformation during each eruption.

318

319 **Declarations**

320

321 **Ethics approval and consent to participate**

322 Not applicable.

323

324 **Consent for publication**

325 Not applicable.

326

327 **List of abbreviations**

328 bsl: below sea level; SVRC: Sakurajima Volcano Research Center; MLIT: Ministry of
329 Land, Infrastructure, Transport and Tourism of Japan; JMA: Japan Meteorological
330 Agency; c-AIC: correction of Akaike's Information Criterion; AIC: Akaike's Information
331 Criterion; GPS: Global Positioning System; DEM: digital elevation model

332

333 **Availability of data and materials**

334 The datasets supporting the conclusions of this article are included within the article.

335

336 **Competing interests**

337 The authors declare that they have no competing interests.

338

339 **Funding**

340 This study was supported by the Ministry of Education, Culture, Sports, Science and
341 Technology (MEXT) of Japan, under its Earthquake and Volcano Hazards Observation
342 and Research Program, and was a consignment study from the Ministry of Land,
343 Infrastructure, Transport and Tourism of Japan (MLIT).

344

345 **Author's contributions**

346 KH contributed to the study conception and design; acquisition, analysis and
347 interpretation of the data; and drafted the manuscript. MI contributed to the study

348 conception and design; acquisition and analysis of data; and helped to draft the manuscript
349 with critical revisions.

350

351 **Acknowledgements**

352 We used tilt and strain data from the AVOT station and DEM data from the Osumi
353 Office of River and National Highway, Kyushu Regional Development Bureau, MLIT;
354 tilt data from the JMA; and the program code of Dr. Carroll's FORTRAN genetic
355 algorithm driver (Carroll, 1999). Some of the figures in this paper were prepared using
356 generic mapping tools (Wessel et al., 2013). We would like to thank Dr. Hickey and an
357 anonymous reviewer for their helpful comments.

358

359 **References**

360 Akaike H (1973) Maximum likelihood identification of Gaussian autoregressive moving
361 average model. *Biometrika*, 60, 2, 255, doi:10.2307/2334537.

362 Árnadóttir T, Segall P (1994) The 1989 Loma Prieta earthquake imaged from inversion
363 of geodetic data. *J. Geophys. Res.*, 99 (B11), 21,835-21,855, doi:10.1029/94JB01256.

364 Battaglia M, Cervelli PF, Murray JR (2013) Modeling crustal deformation near active
365 faults and volcanic centers—a catalog of deformation models, USGS Numbered
366 Series, Technique and Methods, 13, p. B1, doi:10.3133/tm13B1.

367 Carroll DL (1999) FORTRAN genetic algorithm (GA) driver.
368 [http://www.cuaerospace.com/Technology/GeneticAlgorithm/GADriverFreeVersion.](http://www.cuaerospace.com/Technology/GeneticAlgorithm/GADriverFreeVersion.aspx)
369 [aspx](http://www.cuaerospace.com/Technology/GeneticAlgorithm/GADriverFreeVersion.aspx). Accessed 7 June 2020.

370 Currenti G, Del Negro C, Ganci G (2007) Modeling of ground deformation and gravity
371 fields using finite element method: an application to Etna volcano. *Geophys. J. Int.*,

372 169, 775–786, doi:10.1111/j.1365-246X.2007.03380.x.

373 Del Negro C, Currenti G, Scandura D (2009) Temperature-dependent viscoelastic
374 modeling of ground deformation: Application to Etna volcano during the 1993-1997
375 inflation period. *Phys. Earth Planet. Inter.*, 172, 299–309, doi:
376 10.1016/j.pepi.2008.10.019.

377 Eto K (1989) Ground deformation at Sakurajima and around Aira caldera associated with
378 the volcanic activity. *Ann. Disaster Prev. Res. Inst., Kyoto Univ.*, 32 (B-1), 29-39 (in
379 Japanese with English abstract).

380 Fialko Y, Y Khazan, M Simons (2001) Deformation due to a pressurized horizontal
381 circular crack in an elastic half-space, with applications to volcano geodesy, *Geophys.*
382 *J. Int.*, 146, 181-190, doi:10.1046/j.1365-246X.2001.00452.x.

383 Gottsmann J., Odbert H. (2014) The effects of thermomechanical heterogeneities in island
384 arc crust on time-dependent preeruptive stresses and the failure of an andesitic
385 reservoir. *J. Geophys. Res. Solid Earth*, 119, 4626-4639, doi:10.1002/2014JB011079.

386 Hickey J, Gottsmann J, Nakamichi H, Iguchi M (2016) Thermomechanical controls on
387 magma supply and volcanic deformation: application to Aira caldera, Japan. *Sci. Rep.*
388 6, 32691.

389 Hotta K, Iguchi M, Ohkura T, Yamamoto K (2016a) Multiple-pressure-source model for
390 ground inflation during the period of high explosivity at Sakurajima volcano, Japan
391 – Combination analysis of continuous GNSS, tilt and strain data –, *J. Volcanol.*
392 *Geotherm. Res.*, 310, 12-25, doi:10.1016/j.jvolgeores.2015.11.017.

393 Hotta K, Iguchi M, Tameguri T (2016b) Rapid dike intrusion into Sakurajima volcano on
394 August 15, 2015, as detected by multi-parameter ground deformation observations,
395 *Earth, Planets and Space*, 68, 68, doi:10.1186/s40623-016-0450-0.

- 396 Iguchi M (1994) A Vertical Expansion Source Model for the Mechanisms of Earthquakes
397 Originated in the Magma Conduit of an Andesitic Volcano: Sakurajima, Japan. Bull.
398 Volcanol. Soc. Japan, 39, 2, 49–67, doi:10.18940/kazan.39.2_49.
- 399 Iguchi M, Tameguri T, Ohta Y, Ueki S, Nakao S (2013) Characteristics of Volcanic
400 Activity at Sakurajima Volcano's Showa Crater During the Period 2006 to 2011. Bull.
401 Volcanol. Soc. Japan, 58, 1, 115–135, doi:10.18940/kazan.58.1_115.
- 402 Ishihara K (1981) A quantitative relation between the ground deformation and the
403 volcanic materials ejected. Abstract 1981 IAVCEI Symposium – Arc Volcanism, 143.
- 404 Ishihara K (1990) Pressure sources and induced ground deformation associated with
405 explosive eruptions at an andesitic volcano: Sakurajima volcano, Japan. Magma
406 transport and storage (Ed. M.P. Ryan), John Willey and Sons, 335–356.
- 407 McTigue DF (1987) Elastic stress and deformation near a finite spherical magma body:
408 Resolution of the point source paradox. J. Geophys. Res., 92, B12, 12031–12940,
409 doi:10.1029/JB092iB12p12931.
- 410 Miyamachi H, Tomari C, Yakiwara H, Iguchi M, Tameguri T, Yamamoto K, Ohkura T,
411 Ando T, Onishi K, Shimizu H, Yamashita Y, Nakamichi H, Yamawaki T, Oikawa J,
412 Ueki S, Tsutsui T, Mori H, Nishida M, Hiramatsu H, Koeda T, Masuda Y, Katou K,
413 Hatakeyama K, Kobayashi T (2013) Shallow Velocity Structure Beneath the Aira
414 Caldera and Sakurajima Volcano as Inferred from Refraction Analysis of the Seismic
415 Experiment in 2008. Bull. Volcanol. Soc. Japan, 58(1), 227–237.
- 416 Mogi K (1958) Relations between the Eruptions of Various Volcanoes and the
417 Deformations of the Ground Surfaces around them. Bull. Earthq. Res. Inst. Univ.
418 Tokyo, 36, 99–134.
- 419 Okada Y (1992) Internal deformation due to shear and tensile faults in a half space. Bull.

420 Seismol. Soc. Am, 82(2), 1018–1040.

421 Pascal K, Neuberg J, Rivalta E (2014) On precisely modelling surface deformation due
422 to interacting magma chambers and dikes. *Geophys. J. Int.*, 196, 253–278, doi:
423 10.1093/gji/ggt343.

424 Rivalta E, Segall P (2008) Magma compressibility and the missing source for some dike
425 intrusions. *Geophys. Res. Lett.*, 35, 1–5, doi:10.1029/2007GL032521.

426 Sugiura N (1978) Further analysis of the data by Akaike’s information criterion and the
427 finite corrections. *Communications in Statistics - Theory and Methods*, 7(1), 13-26,
428 doi:10.1080/03610927808827599.

429 Tateo Y, Iguchi M (2009) Ground Deformation Associated with BL-type Earthquake
430 Swarms at Sakurajima Volcano. *Bulletin of Volcanological Society of Japan*, 54(4),
431 175-186. (in Japanese with English abstract)

432 Tiampo KF, Rundle JB, Fernandez J, Langbein JO (2000) Spherical and ellipsoidal
433 volcanic sources at Long Valley caldera, California, using a genetic algorithm
434 inversion technique, *J. Volcanol. Geotherm. Res.*, 102, 189–206, doi:
435 10.1016/S0377-0273(00)00185-2.

436 Tsutsui T, Iguchi M, Tameguri T, Nakamichi H (2016) Structural evolution beneath
437 Sakurajima Volcano, Japan, revealed through rounds of controlled seismic
438 experiments. *Journal of Volcanology and Geothermal Research*, 315, 1-14, doi:
439 10.1016/j.jvolgeores.2016.02.008.

440 Wessel P, Smith WHF, Scharroo R, Luis JF, Wobbe F (2013) Generic Mapping Tools:
441 Improved Version Released. *EOS Trans. Am. Geophys. Union*, 94, 409–410,
442 doi:10.1002/2013EO450001.

443 Williams CA, Wadge G (1998) The effects of topography on magma chamber

444 deformation models: Application to Etna and radar interferometry. *Geophys. Res.*
445 *Lett.*, 25(10), 1549–1552, doi:10.1029/98GL01136.

446 Yamamoto K, Sonoda T, Takayama T, Ichikawa N, Ohkura T, Yoshikawa S, Hiroyuki I,
447 Matsushima T, Uchida K, Nakamoto M (2013) Vertical ground deformation
448 associated with the volcanic activity of Sakurajima volcano, Japan during 1996–2010
449 as revealed by repeated precise leveling surveys. *Bulletin of Volcanological Society*
450 *of Japan*, 58(1), 137-151.

Figures

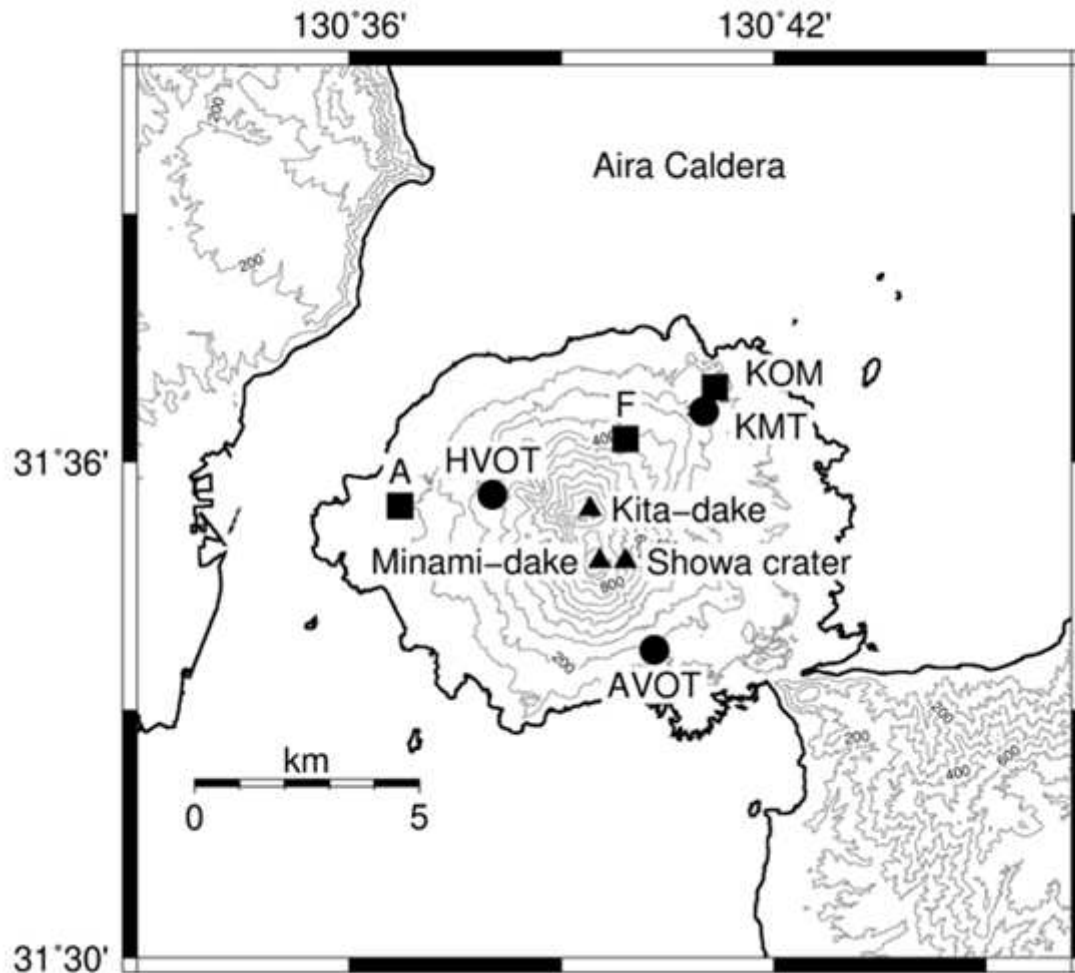


Figure 1

Distribution of tilt and strain stations used in the present study. The solid circles represent the Arimura (AVOT), Harutayama (HVOT) and Komen (KMT) observation tunnels where tiltmeters and strainmeters are located. The solid squares represent borehole tiltmeters of the Japan Meteorological Agency at Yokoyama (A) and Amida-gawa (F), and that of the Sakurajima Volcano Research Center of Kyoto University at Komen (KOM). The solid triangles represent the summit craters of Kita-dake and Minami-dake, and the Showa crater.

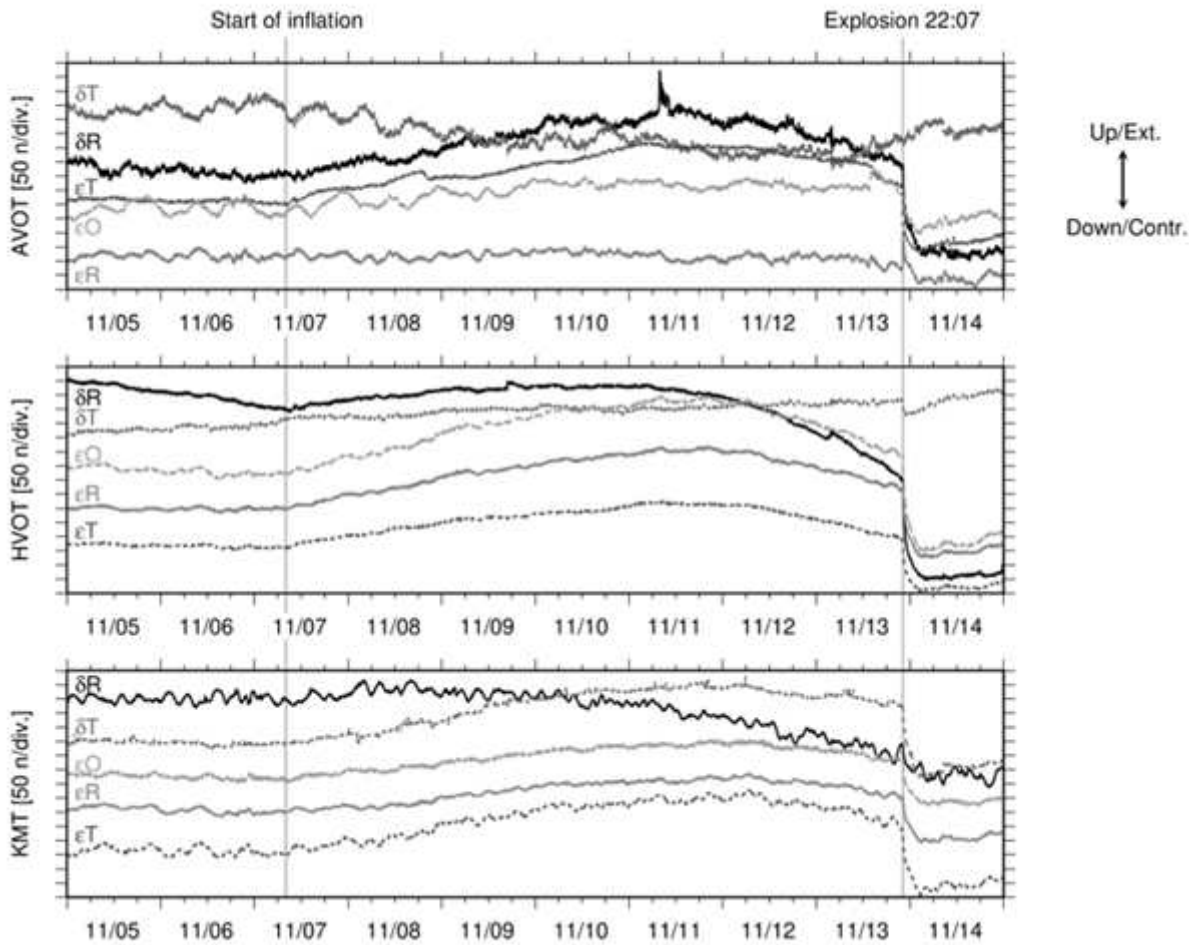


Figure 2

Tilt and strain records at the AVOT, HVOT and KMT stations during the period from November 5 through 14, 2017. δR and δT represent radial and tangential tilt changes, respectively. ϵR , ϵT and ϵO are strain changes in the radial, tangential and oblique components, respectively. The increase in the tilt represents an upward change in a direction toward the Minami-dake crater in the radial component and in a direction rotated clockwise 90° from the crater in the tangential component, respectively. The increase in the strain represents an extension of the radial component in a direction toward the crater and direction rotated clockwise 90° and 45° from the crater in the tangential and oblique components, respectively. The vertical gray lines represent the start of inflation on November 7, 2017 and the onset of the explosion at Minami-dake on November 13, 2017, respectively.

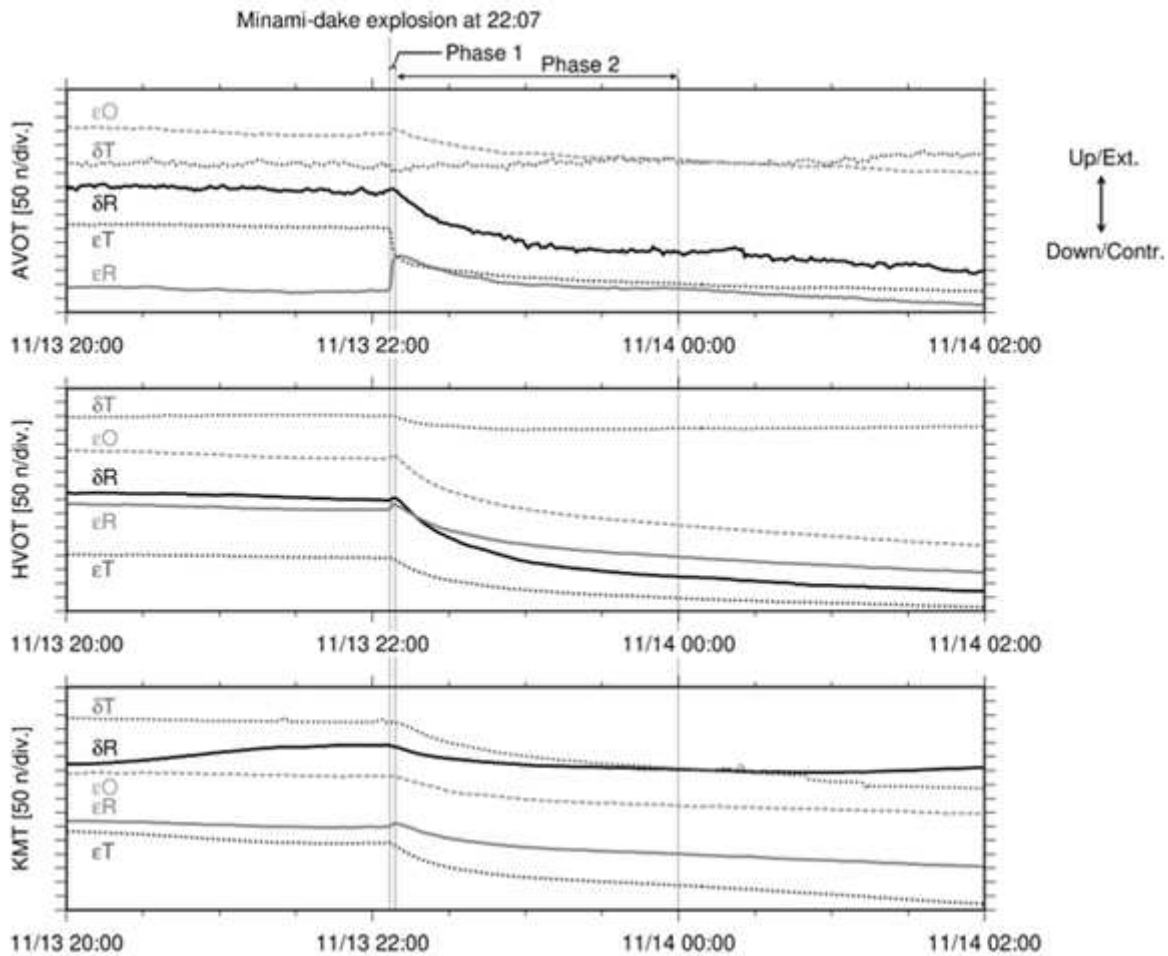


Figure 3

Magnification of Fig. 2 for the period from November 13, 2017, 20:00 through 2:00 of the following day. The symbols are the same as in Fig. 2(a). Phases 1 and 2 are the periods 22:07–22:10 and 22:10–24:00 of November 13, 2017, respectively.

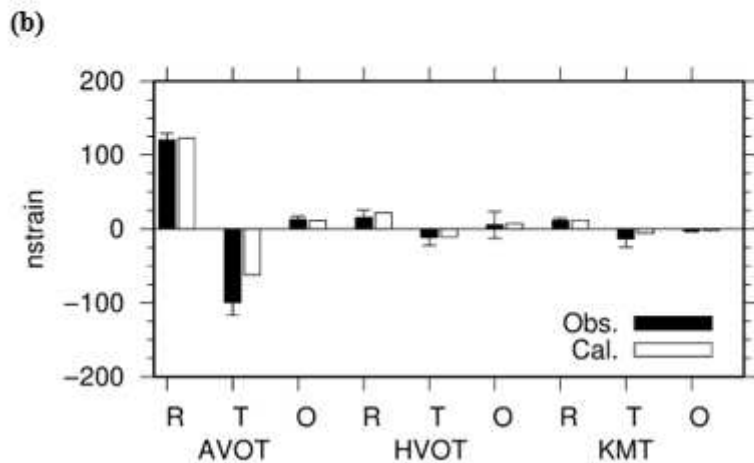
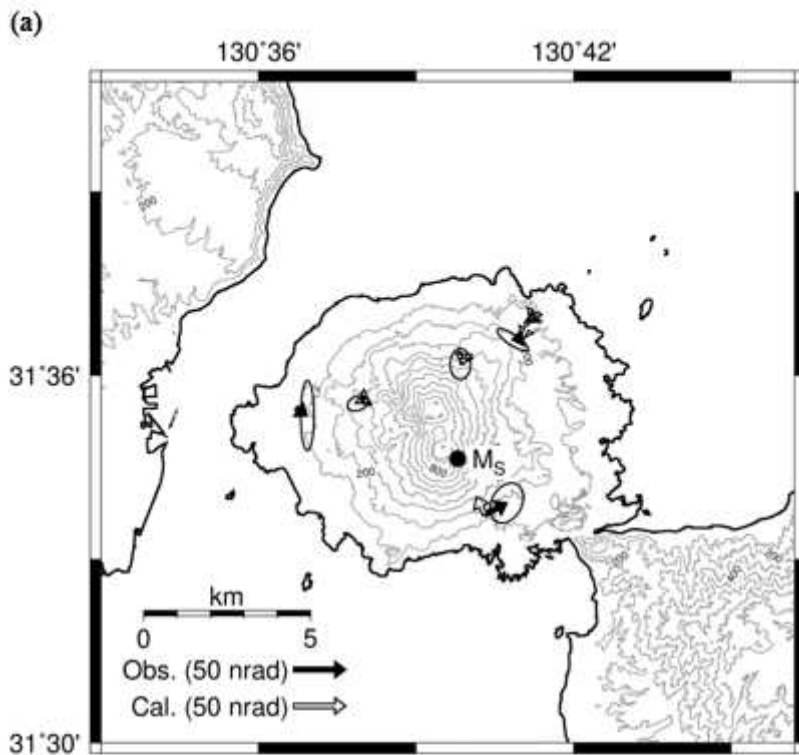


Figure 4

(a) Location of the obtained spherical source (MS, the solid circle) for phase 1 (22:07–22:10) and a comparison of the observed (black) and calculated (white) downward tilts. The error ellipses are 3σ . The 99% confidence level estimated by an F-test (Árnadóttir and Segall, 1994) is within the size of the solid circle. The depth of the source MS is 0.1 km bsl. (b) Comparison of the observed (black) and calculated (white) radial (R), tangential (T) and oblique (O) extensions. The error bars are 3σ .

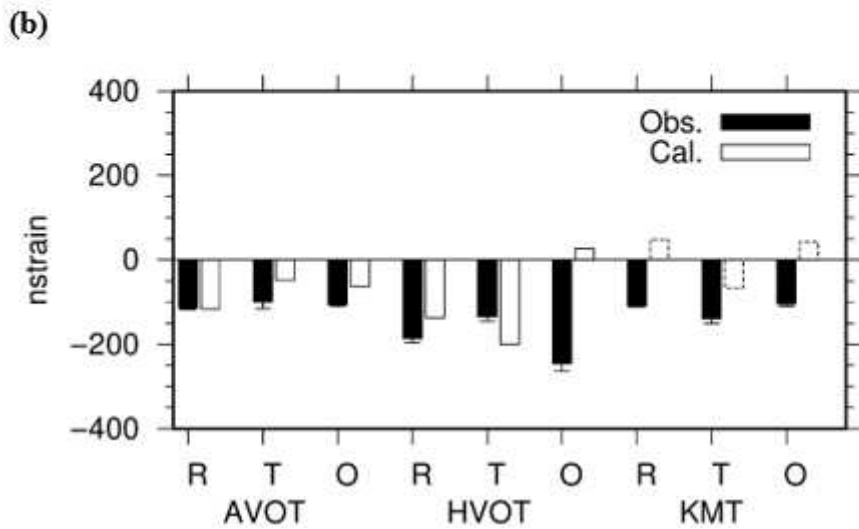
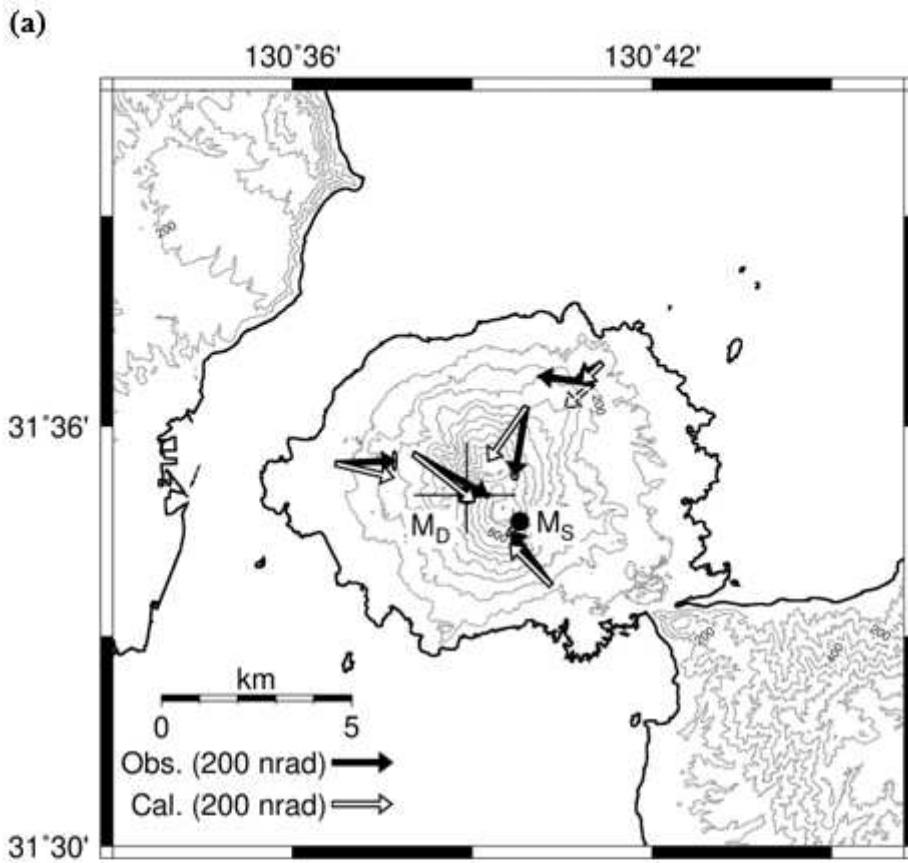


Figure 5

Same as Fig. 4, but for phase 2 (22:10–24:00), excluding the data of KMT and assuming dual spherical sources (source M_S obtained for phase 1 and an additional deeper spherical source M_D). The depths of the source M_S and M_D are 0.1 km bsl and 3.3 km bsl, respectively. The error bar is the 99% confidence level estimated by an F-test (Árnadóttir and Segall, 1994).

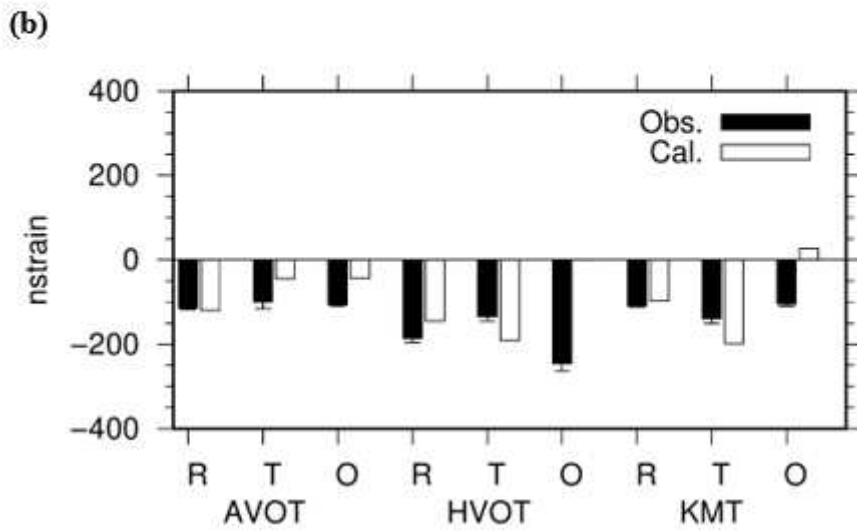
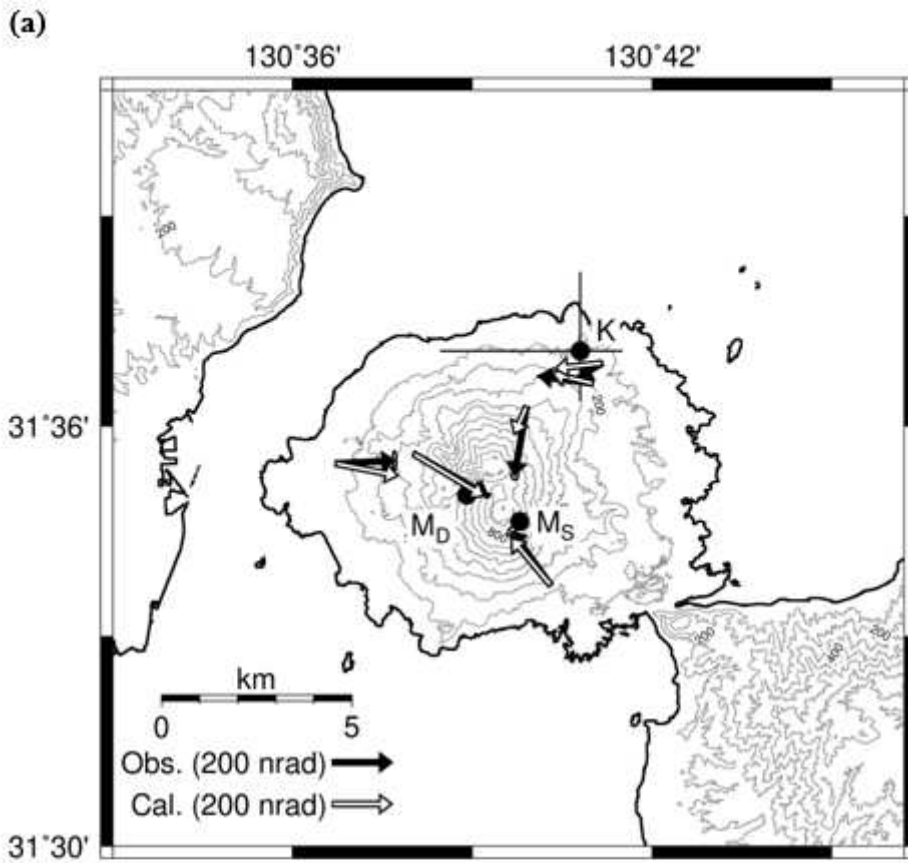


Figure 6

Same as Fig. 4, but assuming three spherical sources (the dual Minami-dake sources MS and MD and an additional spherical source K) for all the data including KMT. The depths of the sources MS, MD and K were 0.1 km bsl, 3.3 km bsl and 3.2 km bsl, respectively.

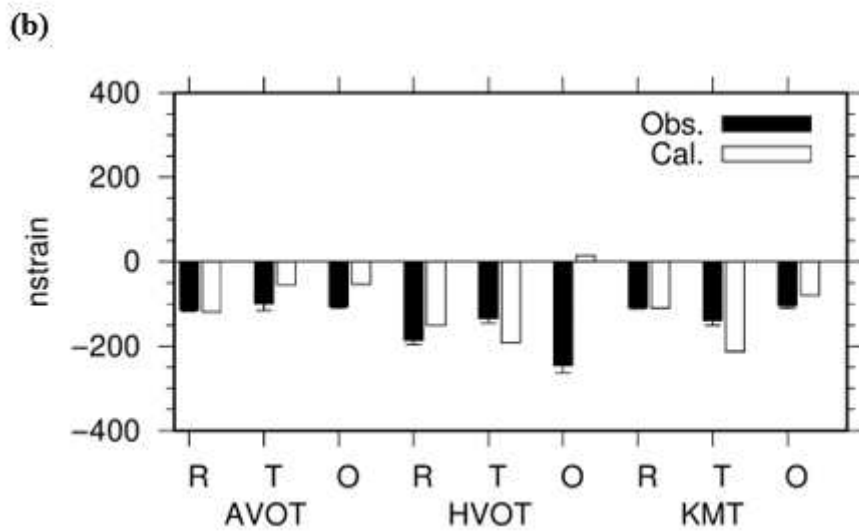
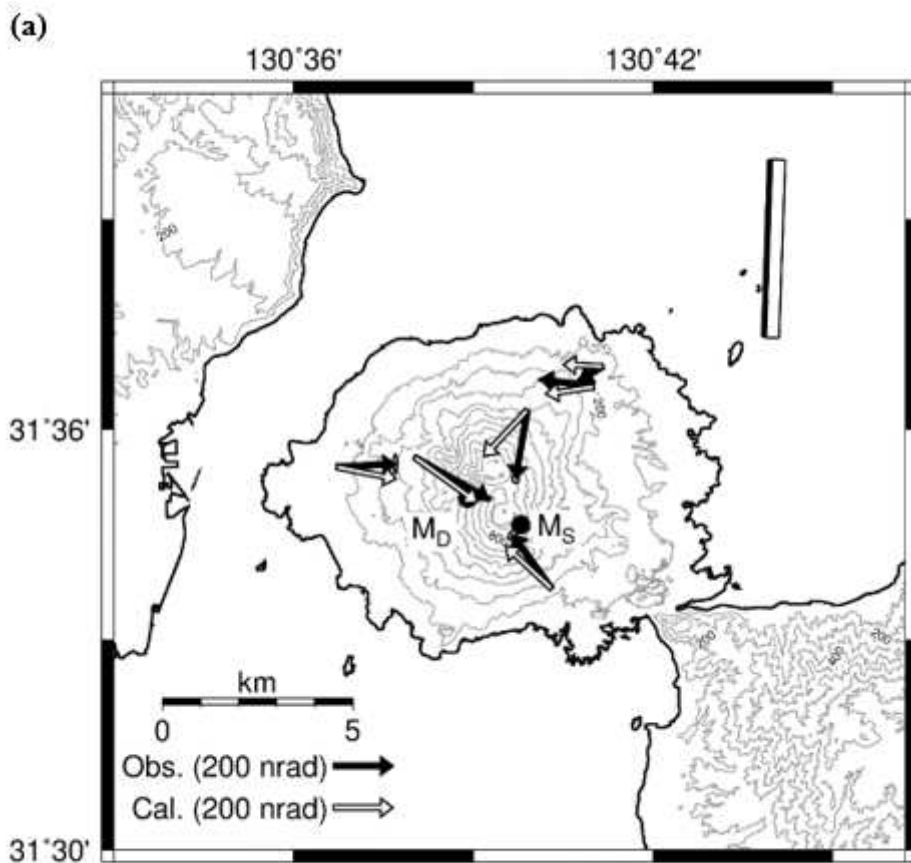


Figure 7

Same as Fig. 4, but assuming the dual Minami-dake sources MS and MD and an additional dislocation source model (rectangle). The thick black line of the rectangle represents the top of the obtained dislocation source model. The depths of the sources MS, MD and the top of the dislocation source are 0.1 km bsl, 3.3 km bsl and 0.7 km bsl, respectively.

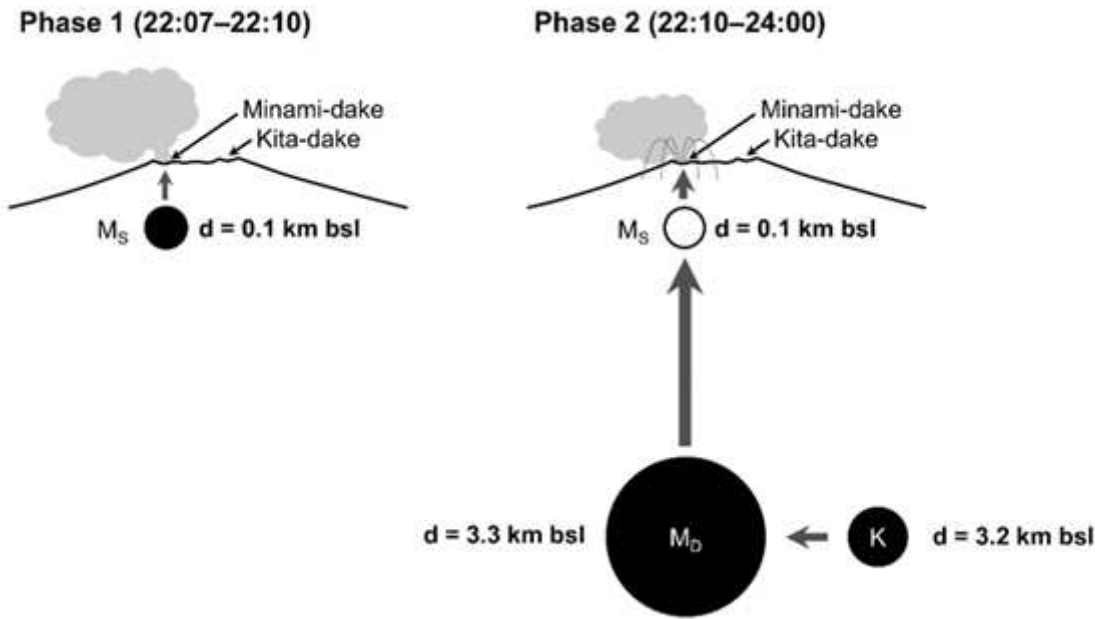


Figure 8

Schematic diagrams of magma migration during the Minami-dake explosion revealed in the present study. The left diagram represents phase 1 (22:07–22:10) and the right represents phase 2 (22:10–24:00). The open and solid circles represent inflation and deflation of the spherical sources, respectively. The thickness of the arrows between each source or the Minami-dake crater represents the amount of magma migration based on the assumptions that uncompressible magma migrates from sources K to MD, MD to MS, and MS to Minami-dake crater, and magma don't inject toward the source K.

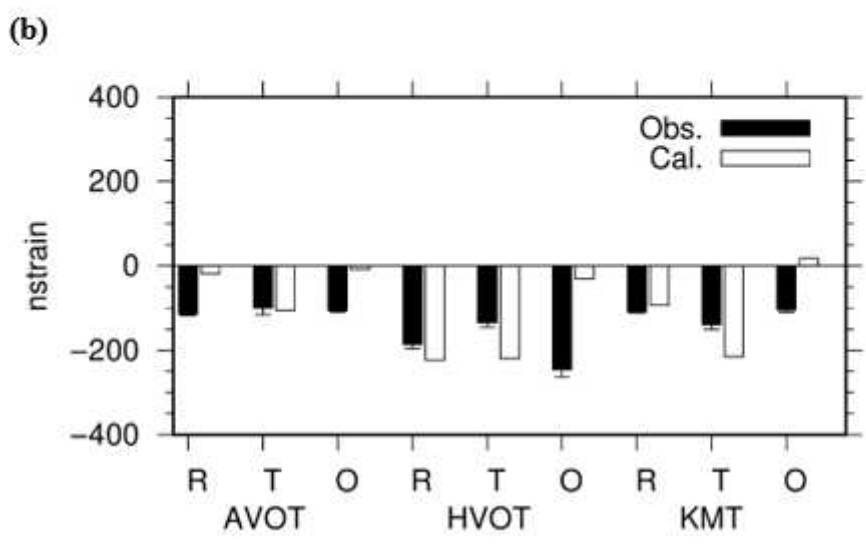
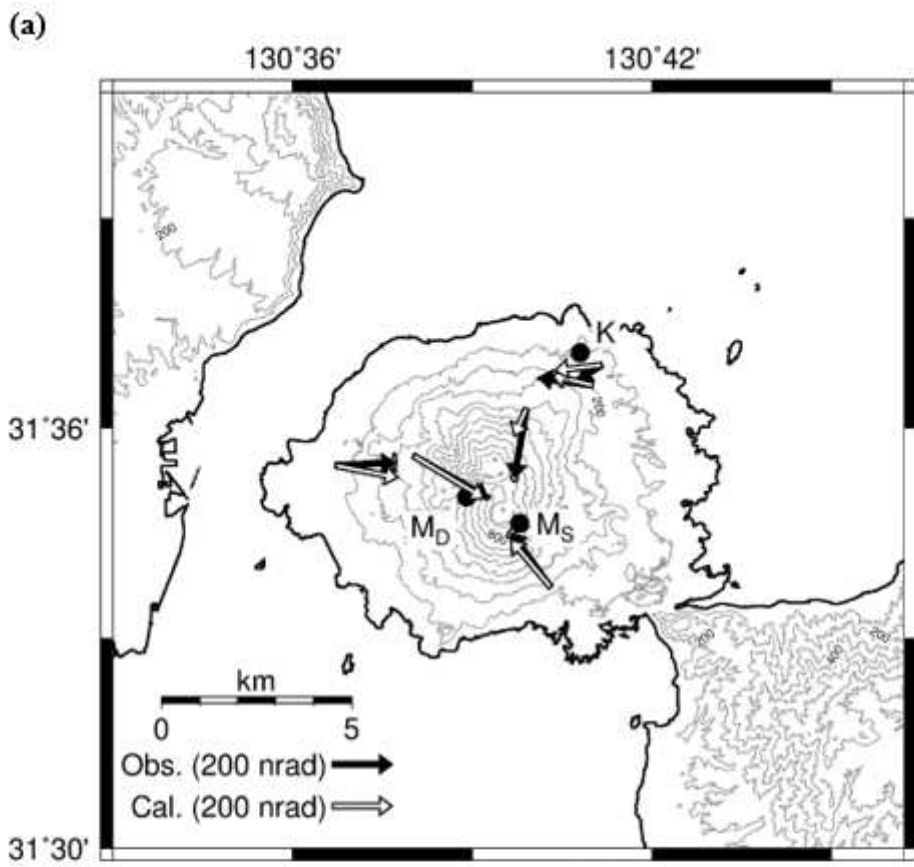


Figure 9

Same as Fig. 6, but for the analysis using finite element method in section 5.3.